JACS
JOURNAL OF THE AMERICAN CHEMICAL SOCIETY
Article
Cite This: J. Am. Chem. Soc. 2019, 141, 2128−2134
pubs.acs.org/JACS

Millimeter-Scale Single-Crystalline Semiconducting $MoTe_2$ via Solid-to-Solid Phase Transformation

Xiaolong Xu,[†,§] Shulin Chen,[‡] Shuai Liu,[†] Xing Cheng,[†] Wanjin Xu,[†] Pan Li,[†] Yi Wan,[†] Shiqi Yang,[†,∥] Wenting Gong,[†] Kai Yuan,[†] Peng Gao,[§,‡,⊥] Yu Ye,*[,†,§] and Lun Dai*[,†,§]

[†]State Key Lab for Artificial Microstructure & Mesoscopic Physics, School of Physics, Peking University, Beijing 100871, China
[§]Collaborative Innovation Center of Quantum Matter, Beijing 100871, China
[‡]Electron Microscopy Laboratory, School of Physics, Peking University, Beijing 100871, China
[∥]Academy for Advanced Interdisciplinary Studies, Peking University, Beijing 100871, China
[⊥]International Center for Quantum Materials, School of Physics, Peking University, Beijing 100871, China

Supporting Information

ABSTRACT: Among the Mo- and W-based two-dimensional (2D) transition metal dichalcogenides, $MoTe_2$ is particularly interesting for phase-engineering applications, because it has the smallest free energy difference between the semiconducting 2H phase and metallic 1T′ phase. In this work, we reveal that, under the proper circumstance, Mo and Te atoms can rearrange themselves to transform from a polycrystalline 1T′ phase into a single-crystalline 2H phase in a large scale. We manifest the mechanisms of the solid-to-solid transformation by conducting density functional theory calculations, transmission electron microscopy, energy dispersive X-ray spectroscopy, X-ray photoelectron spectroscopy, and Raman spectroscopy. The phase transformation is well described by the time−temperature−transformation diagram. By optimizing the kinetic rates of nucleation and crystal growth, we have synthesized a single-crystalline 2H-$MoTe_2$ domain with a diameter of 2.34 mm, a centimeter-scale 2H-$MoTe_2$ thin film with a domain size up to several hundred micrometers, and a seamless 1T′−2H $MoTe_2$ coplanar homojunction. The 1T′−2H $MoTe_2$ homojunction provides an elegant solution for ohmic contact of 2D semiconductors. The controlled solid-to-solid phase transformation in 2D limit provides a new route to realize wafer-scale single-crystalline 2D semiconductor and coplanar heterostructure for 2D circuitry.

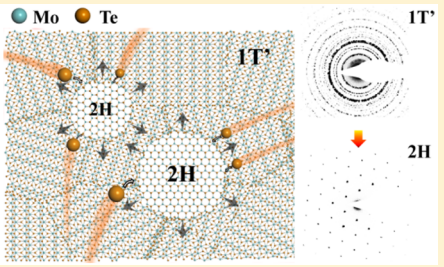

INTRODUCTION

Due to their atomic thickness and nonzero band gap, two-dimensional (2D) transition metal dichalcogenide (TMDC) semiconductors have kept a promise for the scaling of transistors.[1,2] However, fundamental challenges related to contacts of 2D semiconductors often limit their ultimate device performance.[3] For example, metals deposited on the 2D semiconductors form high-resistance contacts, due to Fermi level pinning.[4] Recently, contacting 2D semiconductors using coplanar metallic 2D materials has shown promise in solving the problematic high-resistance contacts of 2D semiconductors.[5−8] Reduced contact resistances were observed in metallic 1T-MoS_2/semiconducting 2H-MoS_2 and metallic 1T′-$MoTe_2$/semiconducting 2H-$MoTe_2$ coplanar heterostructures with seamless interfaces,[5,6] which were fabricated using intercalation and laser heating induced phase transformation methods, respectively. Nevertheless, directly growing coplanar metallic and semiconducting TMDCs in a large scale is significantly important for practical applications.[7] Among the Mo- and W-based TMDCs, $MoTe_2$ is particularly interesting for phase-engineering applications, because it has the smallest free energy difference between the semiconducting 2H phase and metallic 1T′ phase.[9] This small energy difference (∼40 meV per $MoTe_2$ formula unit)[10] leads to the possibility of phase-controlled synthesis in a large scale. Although the controlled synthesis of large-area 1T′- and 2H-$MoTe_2$ thin films has made rapid progress,[11−17] many open questions remain, such as what are the driving force and kinetics for the phase transformation? How large of a semiconducting 2H-$MoTe_2$ single-crystalline domain could be achieved? What is the relationship between the nucleation density and growth rate of the 2H domains? How is the contact between the 1T′- and 2H-$MoTe_2$ in the coplanar homojunction? Fully understanding the phase transformation mechanism, as well as controlling the phase transformation parameters, is crucial for practical applications of $MoTe_2$ materials.

In this work, we study the solid-to-solid phase transformation from the metallic 1T′-$MoTe_2$ to semiconducting 2H-$MoTe_2$ in detail. The driving force and kinetics of the phase transformation are revealed. By tuning the relationship between the kinetic rates of 2H-$MoTe_2$ nucleation and crystal growth, we are able to synthesize a single-crystalline 2H-$MoTe_2$ domain with a diameter of 2.34 mm, centimeter-scale

Received: November 14, 2018
Published: January 11, 2019

DOI: 10.1021/jacs.8b12230
J. Am. Chem. Soc. 2019, 141, 2128−2134

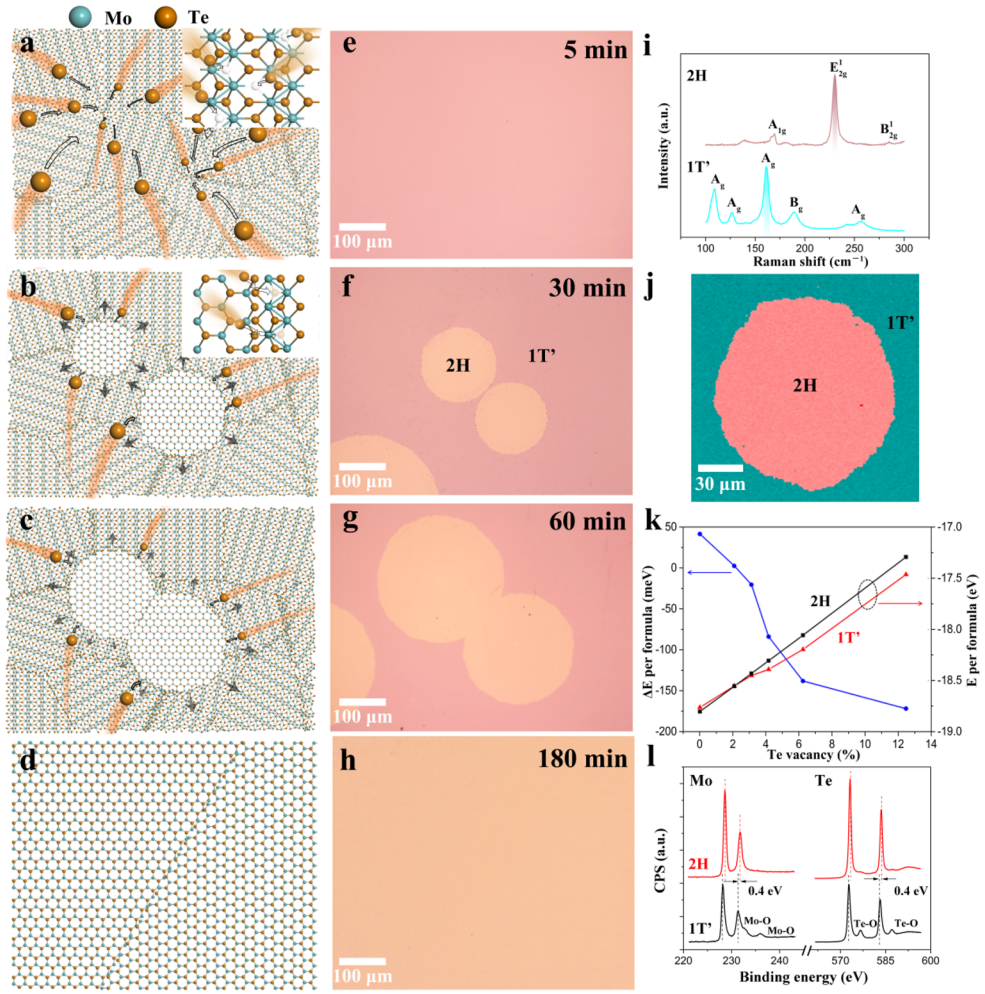

Figure 1. (a–d) Schematic diagrams of the phase transformation from 1T′- to 2H-$MoTe_2$ film. (a) 1T′ phase polycrystalline $MoTe_2$ film with Te vacancies. The Te atoms in ambient tend to occupy the vacancies, which induces the phase transformation. (b) As Te atoms occupy the vacancies in the 1T′ phase film, there is a phase transformation into a circle, where the recrystallization occurs at the boundary of 1T′-$MoTe_2$ and 2H-$MoTe_2$. (c) As growth time proceeds, the phase transformation frontiers from two neighboring 2H circles meet and form a seamless grain boundary. (d) All the circles merge together and become a uniform 2H phase $MoTe_2$ film. (e–h) Optical images of the $MoTe_2$ films grown under different growth times. (i) Raman spectra inside (brown line) and outside (cyan line) the circle, which correspond to 2H- and 1T′-$MoTe_2$, respectively. (j) Raman mapping image of the E^1_{2g} mode of 2H-$MoTe_2$ and the A_g mode of 1T′-$MoTe_2$ (labeled by the corresponding shadow areas in i). (k) DFT calculations of the energy per formula of 1T′ $MoTe_2$ (red line) and 2H $MoTe_2$ (black line) versus the concentration of Te vacancies. The blue line corresponds to the energy difference of the two phases under different concentrations of Te vacancies. 1T′ becomes more stable when the Te vacancy concentration is larger than 2%. (l) High-resolution XPS of the Mo 3d and Te 3d core levels of the 2H- (red lines) and the 1T′-$MoTe_2$ (black lines).

2H-$MoTe_2$ thin films with a domain size up to hundreds of micrometers, and the seamless 1T′–2H $MoTe_2$ coplanar homojunction. The phase transformation occurring at different temperatures is well described by the developed analytic equations. The partially phase transformed $MoTe_2$ film naturally forms a seamless 1T′–2H interface. The coplanar 1T′–2H–1T′ $MoTe_2$ field-effect transistor (FET) shows ohmic contact characteristics and an enhanced field-effect mobility of 30 $cm^2\ V^{-1}\ s^{-1}$ at room temperature.

RESULTS AND DISCUSSION

We employed chemical vapor deposition (CVD) to phase controllably synthesize $MoTe_2$ film in a large scale. In order to get insight into the solid-to-solid phase transformation mechanism of the $MoTe_2$ film, a time-evolution experiment was conducted. First, a 1–1.5 nm thick Mo film was prepared on the Si/SiO_2 substrate via magnetron sputtering. Then, the $MoTe_2$ films with different phases were grown by tellurizing the Mo film at 620 °C under different growth times. At a short growth time of 5 min (Figure 1a and e), the Mo thin film was fully tellurized and formed 1T′ phase $MoTe_2$, which is confirmed by the well-resolved A_g (107 cm^{-1}), A_g (127 cm^{-1}), A_g (161 cm^{-1}), and A_g (256 cm^{-1}) Raman signatures (Figure 1i).[18−20] The optical image of the 1T′-$MoTe_2$ shows uniform optical contrast at the centimeter scale (Figure S1). The thickness of the film is about 4.2 nm (Figure S2), corresponding to a six-layer $MoTe_2$.[21] It is worth noting that the inherent metastable 1T′-$MoTe_2$ phase rather than the stable 2H-$MoTe_2$ phase was first formed. Previous calculations reveal that a deficiency of Te is attributed to the formation of this metastable phase by decreasing the free energy of 1T′-$MoTe_2$.[6,10,22,23] Our density functional theory (DFT) calculations confirm that the 1T′ phase is the more stable phase when the Te deficiency exceeds 2% (Figure 1k). When the

DOI: 10.1021/jacs.8b12230
J. Am. Chem. Soc. 2019, 141, 2128–2134

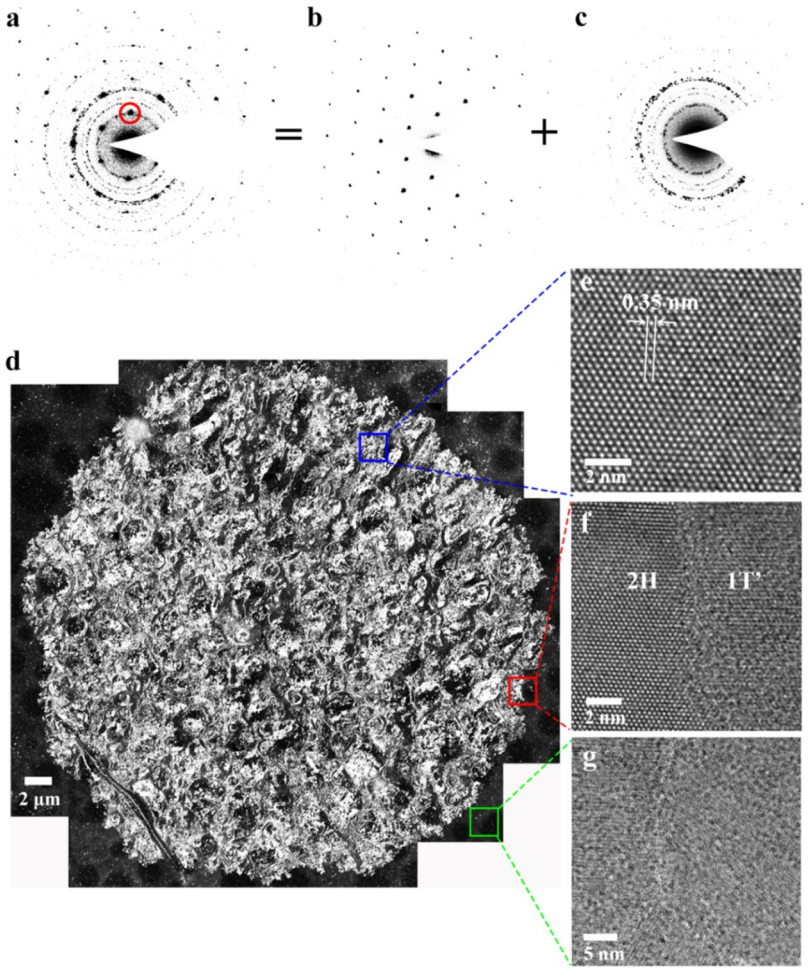

Figure 2. (a) SAED image at the 2H−1T′ boundary. It is composed of a single set of diffraction patterns from the single-crystalline 2H-$MoTe_2$ and a series of diffraction rings from the polycrystalline 1T′-$MoTe_2$. The diffraction spot we use to get the DF-TEM image was labeled by a red circle. (b) SAED image inside the circle, showing a single set of diffraction patterns with 6-fold symmetry corresponding to 2H-$MoTe_2$. (c) SAED pattern outside the circle, showing a series of diffraction rings corresponding to the polycrystalline 1T′-$MoTe_2$. (d) DF-TEM mapping of a complete circle with a diameter of 39 μm (Figure S6). The whole circle shows a strong diffraction signal, indicating that the circular 2H-$MoTe_2$ is single crystalline. (e−g) Corresponding HR-TEM images of the 2H-$MoTe_2$, 2H−1T′ boundary, and the 1T′-$MoTe_2$, respectively. At the 2H−1T′ boundary, 2H-$MoTe_2$ seamlessly stitches to 1T′-$MoTe_2$.

growth time increases to 30 min (Figure 1b and f), some 2H-$MoTe_2$ circles with brighter color emerged and are randomly distributed on the background of the 1T′-$MoTe_2$ film. This is confirmed by the appearance of the out-of-plane A_{1g} (~171 cm^{-1}) and the strong in-plane E^1_{2g} (~234 cm^{-1}) Raman modes (Figure 1i).[24,25] Raman mapping of the representative fingerprints of the 2H-$MoTe_2$ E^1_{2g} mode and 1T′-$MoTe_2$ A_g mode (corresponding to the shadow areas in Figure 1i) clearly shows that both the 2H-$MoTe_2$ circle and 1T′-$MoTe_2$ film are uniform and the interface between them is clear (Figure 1j). As the growth time is prolonged (Figure 1c and g), the 2H-$MoTe_2$ circles grow and come into contact with each other. When the growth time is long enough, all the circles merge together and form a uniform 2H-$MoTe_2$ film (Figure 1d and h). The optical image of the 2H-$MoTe_2$ shows uniform optical contrast at a centimeter scale (Figure S1).

In order to further analyze the stoichiometry of the grown $MoTe_2$ films with different phases, we conducted energy-dispersive X-ray spectroscopy (EDX) and X-ray photoelectron spectroscopy (XPS) characterizations. The EDX acquired inside and outside the circle reveals that the Te/Mo atomic ratios of 2H-$MoTe_2$ and 1T′-$MoTe_2$ are 1.97 and 1.82, respectively (Figure S3). The XPS spectra of the centimeter-scale 2H- and 1T′-$MoTe_2$ also confirm the presence of Mo and Te. The high-resolution XPS peaks of 2H-$MoTe_2$ are at 228.6 eV (Mo $3d_{5/2}$), 231.8 eV (Mo $3d_{3/2}$), 573.2 eV (Te $3d_{5/2}$), and 583.6 eV (Te $3d_{3/2}$), respectively, while the corresponding peaks of 1T′-$MoTe_2$ red-shift by about 0.4 eV (Figure 1l), agreeing with the previous reports.[6,14,26,27] Besides, the weak shoulder peaks of Mo−O (231.4 and 235.9 eV) and Te−O (576.7 and 587.1 eV) are observed in 1T′-$MoTe_2$, which might result from oxidation of the metastable 1T′-$MoTe_2$.[12,27] The Te/Mo atomic ratio of 1T′-$MoTe_2$ is calculated to be about 1.86, by comparing the area ratio of Mo 3d to Te 3d peaks of 1T′-$MoTe_2$ with those of 2H-$MoTe_2$, assuming the Te/Mo atomic ratio of 2H-$MoTe_2$ is 2. Both the EDX and XPS results show that the 1T′ phase formed in the early stage is a defect-related phase, and in order to facilitate the phase transformation from 1T′- to 2H-$MoTe_2$, a Te-rich environment is needed.

We evaluated the crystallinity of the phase-engineered $MoTe_2$ film using a transmission electron microscope (TEM). The selected-area electron diffraction (SAED) inside the circle with an aperture size of 800 nm (Figure 2b) reveals a

DOI: 10.1021/jacs.8b12230
J. Am. Chem. Soc. 2019, 141, 2128−2134

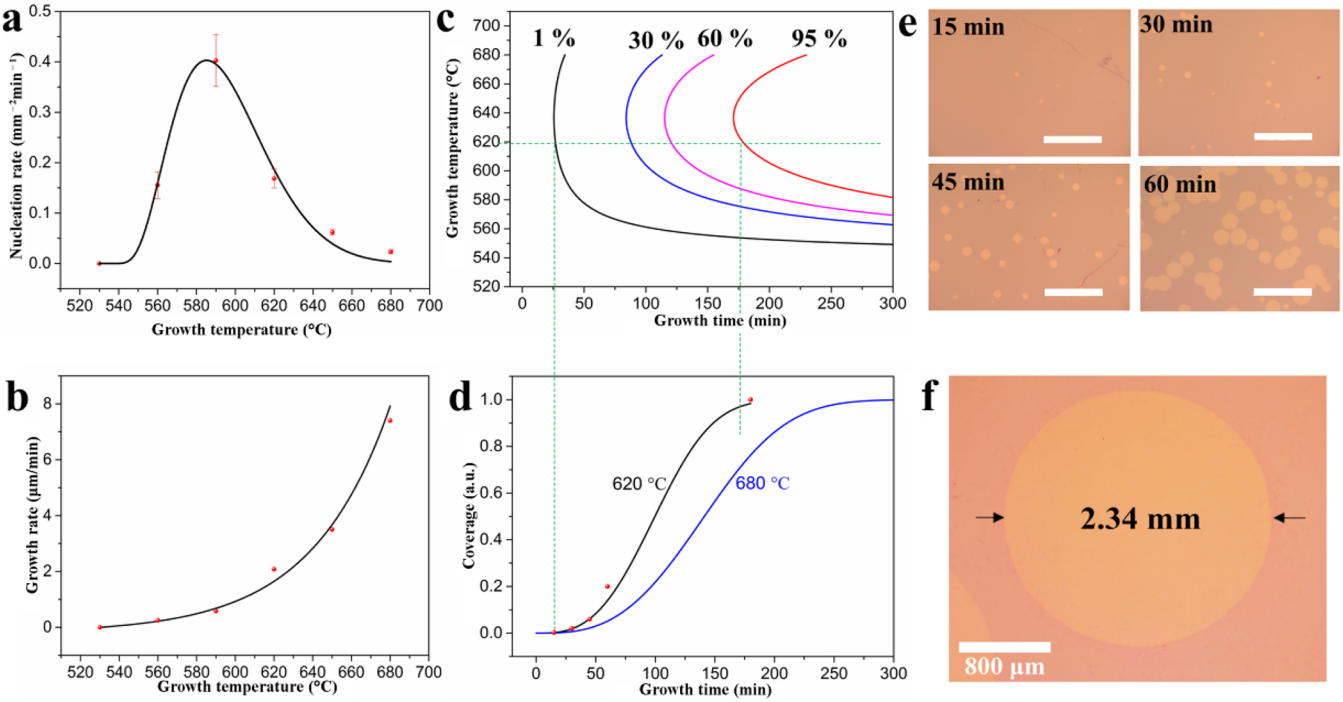

Figure 3. (a, b) Temperature dependences of the nucleation rate and growth rate, respectively. The red dots represent the experimental data. The black curves are the fitting results with eqs 1 and 2, respectively. (c) TTT diagram showing the growth time and temperature relationship with the fraction of 2H-$MoTe_2$ at 1%, 30%, 60%, and 95%, respectively. (d) Fraction of phase transformation versus time for growth temperatures of 620 and 680 °C. Red dots represent the experimental data. (e) Optical images of the $MoTe_2$ samples grown at 620 °C for 15, 30, 45, and 60 min, respectively. The scale bars are 800 μm. (f) Optical image of an isolated few-layer single-crystalline 2H-$MoTe_2$ circle with a diameter of 2.34 mm synthesized with the optimized growth parameters.

single set of diffraction spots with 6-fold symmetry related to the 2H-$MoTe_2$.[14] Correspondingly, the high-resolution TEM (HR-TEM) shows a hexagonal atomic lattice with a spacing distance of 0.35 nm (Figure 2e), consistent with the structure of 2H-$MoTe_2$. In contrast, the SAED pattern taken from the sample outside the circle reveals the polycrystalline nature of the 1T′-$MoTe_2$ film (Figure 2c). The HR-TEM image shows that the polycrystalline film contains monoclinic structure (distorted octahedral or 1T′) domains of about tens of nanometers (Figure 2g and Figure S4).[26] The 1T′ domains show random orientations with respect to 2H-$MoTe_2$ (Figure S5). At their interfaces, the 1T′-$MoTe_2$ stitches seamlessly to 2H-$MoTe_2$ (Figure 2f).

To further investigate the crystallinity of the 2H-$MoTe_2$ circle (Figure S6), we employed the dark-field (DF) technique. A single diffracted spot (labeled by the red circle in Figure 2a) of 2H-$MoTe_2$ was selected using an aperture. Limited by the image size (~8.5 μm × 8.5 μm), 55 DF-TEM images are stitched together to have a full view of a 2H-$MoTe_2$ circle (Figure 2d). DF-TEM, in conjunction with filtered electron diffraction filter domains by crystallographic orientation, was widely used for accurately characterizing grain boundary and grain orientation.[28] The DF-TEM image shows a sharp contrast between 2H- and 1T′-$MoTe_2$ regions, and the bright contrast of the whole circle indicates the single-crystal nature of the 2H-$MoTe_2$. The inhomogeneous contrast inside the circle arises from the adherent particles and wrinkles of the $MoTe_2$ film introduced by the wet transfer process, as well as the carbon film structure of the TEM grid. To further remove doubt caused by the inhomogeneous contrast, we obtain HR-TEM images and corresponding fast Fourier transform (FFT) patterns of four different positions that are 20 μm apart within another 2H phase circle (Figure S7). The fact that all the corresponding FFT patterns do not show any angular variation indicates the lattice orientation is consistent across a large scale. These results reconfirm that the circle is single crystalline. By prolonging the growth time, these single-crystalline 2H circles merge together to form a continuous film. At the boundary of two connecting circles, the HR-TEM and the corresponding FFT patterns show obvious angular deflection of the two circles (Figure S8). It is not surprising that the single-crystalline 2H-$MoTe_2$ domains nucleate with different crystal orientations due to their different local environments. When two circles contact with each other, the phase transformation terminates and a grain boundary forms (Figure S8). Therefore, in order to get a large single-crystalline 2H $MoTe_2$ circle or a high-quality continuous 2H-$MoTe_2$ film with large single-crystal domains, an optimized nucleation density and phase transformation rate are required.

Based on the facts that 2H-$MoTe_2$ and 1T′-$MoTe_2$ have different lattice structures and the domain size of single-crystalline 2H-$MoTe_2$ is much larger than that of 1T′-$MoTe_2$, we can infer that atom rearrangement occurs during the phase transformation from 1T′ to 2H phase. The phase transformation from 1T′- to 2H-$MoTe_2$ could be understood by the relationship between the competing kinetic rates of nucleation and crystal growth, which determines the size distribution of the product. The solid-to-solid phase transformation could be understood by the extended volume concept developed by Kolmogorov, Johnson, Mehl, and Avrami (KJMA) to analyze recrystallization in metals and crystallization in metallic glasses.[29,30] Here, we extend this concept to the 2D case (see Supporting Information Note for details). Thus, the

DOI: 10.1021/jacs.8b12230
J. Am. Chem. Soc. 2019, 141, 2128−2134

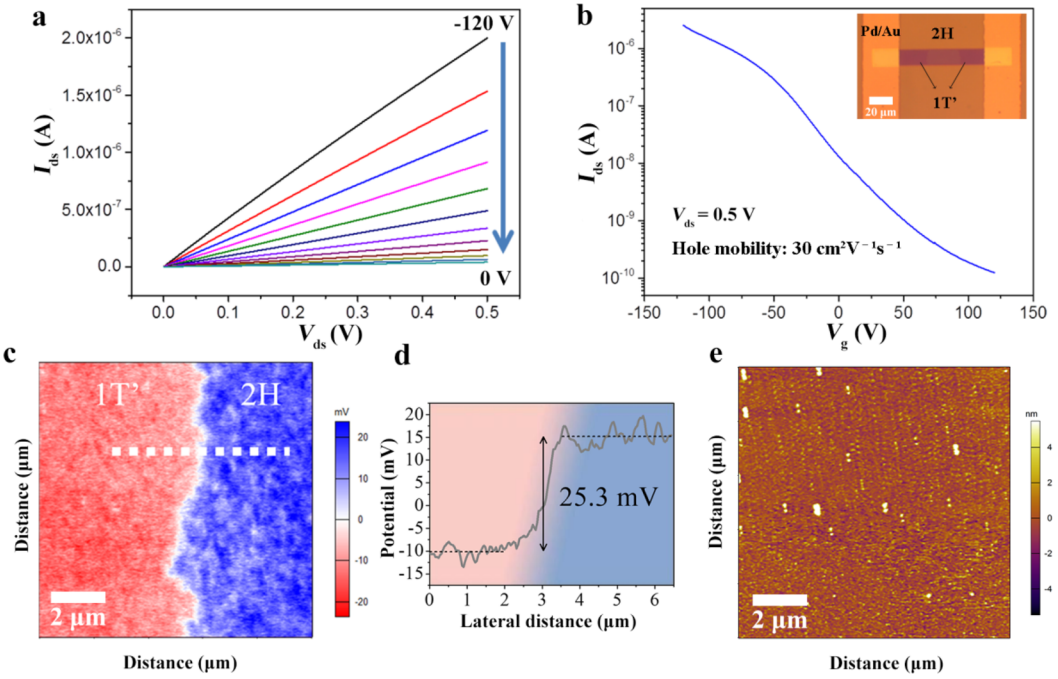

Figure 4. (a) Output characteristics of the coplanar contacted $MoTe_2$ FET under various gate voltages. The linear $I_{ds}-V_{ds}$ characteristic indicates the ohmic contact behavior. (b) Corresponding gate transfer characteristic curve on semilogarithmic scale. The hole mobility is obtained to be about 30 $cm^2\ V^{-1}\ s^{-1}$, using $\mu = (dI_{ds}/dV_g)(L/W)(1/V_{ds}C_g)$, where L, W, and C_g stand for the channel length, channel width, and the gate capacitance per unit area, respectively. The inset image shows the fabricated 1T′−2H−1T′ coplanar FET. (c, d) Surface work function image and the potential line profile, respectively, of the phase transformation boundary, measured by KPFM. The contact barrier height is about 25 meV, which is preferable for the ohmic contact of the p-type 2H-$MoTe_2$. (e) Surface morphology of the same region measured by AFM. The surface is very smooth, and there is no significant height difference across the interface.

nucleation rate I, defined as the number of nuclei formed per unit area in unit time, is given by[31]

$$I = C_0 \exp\left(-\frac{\Delta G^*}{K_b T}\right) f_0 \exp\left(-\frac{\Delta G_m}{K_b T}\right) \quad (1)$$

where C_0 and f_0 are constants, K_b is the Boltzmann constant, T is the temperature, ΔG^* is the activation barrier, and ΔG_m is the diffusion coefficient. In order to get the temperature-dependent nucleation rate, statistical studies at a large scale (30 mm^2) under different growth temperatures were conducted (Figure S9). We can see that the nucleation rate has a maximum value at ∼590 °C (Figure 3a). These results can be well fitted by eq 1 (Figure 3a). As the temperature increases, the terms $\exp(-\frac{\Delta G^*}{K_b T})$ and $\exp(-\frac{\Delta G_m}{K_b T})$ are poles apart. The net effect combining the two terms is that the nucleation rate, I, must go through a maximum. The relatively slow nucleation process appears to be consistent with computation reports showing large barriers for homogeneous 2H−1T′ phase transformation in these materials.[32,33] Once nucleated, the nuclei grow into the surrounding matrix until equilibrium is attained. The atomic rearrangements needed for growth in a congruent phase transformation also involve thermally activated elementary processes (diffusion). Consequently, the growth rate (v) is determined by the rate of diffusion:

$$v = v_0 \exp\left(-\frac{\Delta G_m}{K_b T}\right) \quad (2)$$

where v_0 is a constant. Growth occurs with the same rate in all directions, resulting in a circle shape of a single-crystalline 2H domain. Herein, the growth rate is obtained by dividing the radius of the largest circle with the growth time. The reliability of this method is confirmed by the two-step growth method (Figure S10). The growth rate increases exponentially with temperature, well fitted by eq 2 (Figure 3b). The progress of an isothermal phase transformation can be conveniently represented by plotting the fraction transformation (the fraction of the phase-transformed 2H-$MoTe_2$ over the whole thin film), f, as a function of time and temperature, the so-called time-temperature-transformation (TTT) diagram. We find that, during the phase transformation process, the 2H-$MoTe_2$ nucleates randomly at a constant rate within the 1T′ background (Figure S11). In this case, the $f(t, T)$ is determined by the nucleation rate, the growth rate, and the impingement of adjacent transformed areas, as follows:

$$f = 1 - \exp\left(-\frac{\pi}{3} I v^2 t^3\right) \quad (3)$$

The TTT curves of the phase transformation from 1T′- to 2H-$MoTe_2$ show a typical C shape (Figure 3c), because the driving force for transformation is small at high temperatures, whereas the diffusional coefficient is small at low temperature. The time dependence of phase transformation at a fixed temperature can also be described in terms of the fraction of transformation,[29] which has an S-shape. We performed a systematic time-evolution study of the fraction transformation at 620 °C (Figure 3e). The experimental data (red dots) of the fraction of 2H-$MoTe_2$ are in good agreement with the predicted values by eq 3 (Figure 3d). Temperature has a strong effect on the kinetics of the phase transformation and, therefore, on the fraction of the phase transformation. The S-shaped curve shifts to a longer time region at higher T (Figure

DOI: 10.1021/jacs.8b12230
J. Am. Chem. Soc. 2019, 141, 2128−2134

3d), showing that the transformation is dominated by nucleation and not by diffusion. For example, for transformation that occurs at temperature near melting temperature (T_m), corresponding to low nucleation and high growth rates, fewer nuclei form, but grow more rapidly. Thus, the resulting films consist of fewer and larger 2H-$MoTe_2$ domains. At 700 °C, an isolated single-crystalline 2H-$MoTe_2$ circle with a diameter of 2.34 mm was obtained by 1 h growth (Figure 3f). There is an optimum combination of these two parameters (nucleation and diffusion) with temperature in terms of single-crystalline domain size and rate of transformation. At 660 °C, a continuous 2H-$MoTe_2$ thin film of centimeter scale with a domain size up to hundreds of micrometers was obtained by 3 h growth.

In order to explore the application perspective of the seamless structure of 1T′−2H $MoTe_2$ from solid-to-solid phase transformation, we fabricated and investigated a 1T′−2H−1T′ $MoTe_2$ coplanar homojunction FET (see the Experimental Section for fabrication details). The room-temperature source−drain current (I_{ds}) versus source−drain voltage (V_{ds}) relation shows linear behavior at different gate voltages (Figure 4a), confirming the ohmic contact between the 1T′ and 2H $MoTe_2$. The gate transfer character of the FET shows typical p-type behavior with a high on−off current ratio of ∼1×10^4 (Figure 4b). The hole field-effect mobility (μ) can be obtained to be about 30 $cm^2 V^{-1} s^{-1}$. The obtained mobility is comparable to the exfoliated few-layer 2H-$MoTe_2$ contacted with 1T′-$MoTe_2$ induced by laser heating.[6] A Kelvin probe force microscopy (KPFM) image (Figure 4c) and the potential line profile (Figure 4d) confirm a sharp 25.3 mV potential difference between 1T′- and 2H-$MoTe_2$. The measured higher work function of the 1T′-$MoTe_2$ is preferable for the ohmic contact of the p-type 2H-$MoTe_2$. In contrast, the atomic force microscopy (AFM) height image (Figure 4e) at the same region in Figure 4c show negligible height differences across the interface of 2H−1T′ $MoTe_2$, indicating that they have the same number of layers.

CONCLUSIONS

In conclusion, we have studied the phase transformation from polycrystalline metallic 1T′-$MoTe_2$ to single-crystalline semiconducting 2H-$MoTe_2$ in detail. Upon fully understanding the solid-to-solid phase transformation mechanism, we have synthesized a single-crystalline 2H-$MoTe_2$ domain with a diameter of 2.34 mm, a centimeter-scale 2H-$MoTe_2$ thin film with a domain size up to several hundred micrometers, and a seamless 1T′−2H coplanar heterostructure. The coplanar 1T′−2H−1T′ $MoTe_2$ FET shows ohmic contact characteristics, high on−off ratio, and mobility up to ∼30 $cm^2 V^{-1} s^{-1}$ at room temperature. The controlled solid-to-solid phase transformation in the 2D limit provides a new route to realize a wafer-scale single-crystalline 2D semiconductor and a coplanar heterostructure for next-generation integrated circuits.

EXPERIMENTAL SECTION

Synthesis of the $MoTe_2$ Films. The $MoTe_2$ films were synthesized by tellurizing the Mo film at atmospheric pressure using a horizontal hot-wall tube furnace equipped with mass flow controllers and a vacuum pump. Mo films were deposited on SiO_2/Si substrates through magnetron sputtering. The substrates were placed face-down on an alumina boat containing Te powder placed at the center of the heating zone in a one-inch quartz tube. After evacuating the quartz tube to less than 1 mTorr, we flowed Ar gas at a maximum rate until the pressure reached atmospheric pressure. At atmospheric pressure, Ar and H_2 flowed at rates of 4 and 5 standard cubic centimeters per minute (sccm), respectively. The furnace was ramped to different temperatures in 15 min and was kept at the temperatures for different times to synthesize different phase films. After the reactions, we let the furnace cool to room temperature naturally.

Transfer of the $MoTe_2$ Films. To prepare the sample for TEM and EDX characterizations, the $MoTe_2$ film on the SiO_2/Si substrate was coated with a poly(methyl methacrylate) (PMMA) layer using a spin coater at 3000 rpm for 60 s. After being baked at 100 °C for 2 min, the sample was immersed in a dilute HF solution (1.5%) at room temperature for 10 min. Subsequently, the $MoTe_2$ thin film with PMMA was gently peeled off the SiO_2/Si substrate in water and transferred to a lacey carbon film on a mesh copper grid. Finally, the PMMA was removed using acetone, and the sample was thoroughly rinsed with isopropyl alcohol (IPA).

Fabrication of the Coplanar 1T′−2H−1T′ $MoTe_2$ FET. The $MoTe_2$ film used for fabricating the coplanar 1T′−2H−1T′ FET was synthesized at 590 °C for 60 min. First, we made markers on the film surface with photolithography and a thermal evaporation process. Then the sample was coated with a layer of PMMA followed by a layer of hydrogen silsesquioxane (HSQ) using a spin coater at 2000 and 3000 rpm for 60 s, respectively. A rectangular HSQ protection layer was defined on a 1T′−2H−1T′ region of the sample by electron beam lithography followed by a development process. The exposed PMMA and $MoTe_2$ films were etched by reactive-ion etching (RIE). The gas we used to etch PMMA and $MoTe_2$ films are O_2 and SF_6, respectively. Finally, the remaining rectangular HSQ and PMMA mask was dissolved in acetone, and electrodes (10/50 nm Pd/Au) on 1T′-$MoTe_2$ were made using UV lithography and electron beam evaporation processes.

DFT Calculations. The total energies of both 2H- and 1T′-$MoTe_2$ structures containing 0−13% Te vacancies were calculated by first-principles study based on DFT together with the generalized gradient approximation (GGA) using CASTEP. The positions of Te vacancies in 2H and 1T′ structure models were chosen randomly. All the structures are allowed to relax by minimizing the quantum-mechanical force on each ion site to be less than 0.001 eV/Å.

ASSOCIATED CONTENT

Supporting Information

The Supporting Information is available free of charge on the ACS Publications website at DOI: 10.1021/jacs.8b12230.

Optical images of the centimeter-scale $MoTe_2$ films, AFM image of the $MoTe_2$ film, EDX for 2H- and 1T′-$MoTe_2$, detailed HR-TEM images of $MoTe_2$ film, optical images of $MoTe_2$ film synthesized under different temperatures, nucleation analyses, and TTT diagram in two-dimensional case (PDF)

AUTHOR INFORMATION

Corresponding Authors

*ye_yu@pku.edu.cn
*lundai@pku.edu.cn

ORCID

Yu Ye: 0000-0001-6046-063X
Lun Dai: 0000-0002-6317-6340

Notes

The authors declare no competing financial interest.

ACKNOWLEDGMENTS

This work was supported by the National Natural Science Foundation of China (Nos. 61874003, 11474007, 61521004, 51672007, and 51502007), Beijing Natural Science Foundation (4182028), Nation Key R&D Program of China (Grant

DOI: 10.1021/jacs.8b12230
J. Am. Chem. Soc. 2019, 141, 2128−2134

Nos. 2018YFA0306900 and 2017YFA0206301), the National Basic Research Program of China (No. 2013CB921901), and the "1000 Youth Talent Plan" Fund.

REFERENCES

(1) Desai, S. B.; Madhvapathy, S. R.; Sachid, A. B.; Llinas, J. P.; Wang, Q.; Ahn, G. H.; Pitner, G.; Kim, M. J.; Bokor, J.; Hu, C.; Wong, H. P.; Javey, A. MoS_2 transistors with 1-nanometer gate lengths. *Science* **2016**, *354*, 99−102.

(2) Xu, K.; Chen, D.; Yang, F.; Wang, Z.; Yin, L.; Wang, F.; Cheng, R.; Liu, K.; Xiong, J.; Liu, Q.; He, J. Sub-10 nm nanopattern architecture for 2D material field-effect transistors. *Nano Lett.* **2017**, *17*, 1065−1070.

(3) Schulman, D. S.; Arnold, A. J.; Das, S. Contact engineering for 2D materials and devices. *Chem. Soc. Rev.* **2018**, *47*, 3037−3058.

(4) Allain, A.; Kang, J.; Banerjee, K.; Kis, A. Electrical contacts to two-dimensional semiconductors. *Nat. Mater.* **2015**, *14*, 1195−1205.

(5) Kappera, R.; Voiry, D.; Yalcin, S. E.; Branch, B.; Gupta, G.; Mohite, A. D.; Chhowalla, M. Phase-engineered low-resistance contacts for ultrathin MoS_2 transistors. *Nat. Mater.* **2014**, *13*, 1128.

(6) Cho, S.; Kim, S.; Kim, J. H.; Zhao, J.; Seok, J.; Keum, D. H.; Baik, J.; Choe, D. H.; Chang, K. J.; Suenaga, K.; Kim, S. W.; Lee, Y. H.; Yang, H. Phase patterning for ohmic homojunction contact in $MoTe_2$. *Science* **2015**, *349*, 625−628.

(7) Sung, J. H.; Heo, H.; Si, S.; Kim, Y. H.; Noh, H. R.; Song, K.; Kim, J.; Lee, C. S.; Seo, S. Y.; Kim, D. H.; Kim, H. K.; Yeom, H. W.; Kim, T. H.; Choi, S. Y.; Kim, J. S.; Jo, M. H. Coplanar semiconductor-metal circuitry defined on few-layer $MoTe_2$ via polymorphic heteroepitaxy. *Nat. Nanotechnol.* **2017**, *12*, 1064−1070.

(8) Gong, Y.; Yuan, H.; Wu, C.-L.; Tang, P.; Yang, S.-Z.; Yang, A.; Li, G.; Liu, B.; van de Groep, J.; Brongersma, M. L.; Chisholm, M. F.; Zhang, S.-C.; Zhou, W.; Cui, Y. Spatially controlled doping of two-dimensional SnS_2 through intercalation for electronics. *Nat. Nanotechnol.* **2018**, *13*, 294−299.

(9) Zhou, Y.; Reed, E. J. Structural Phase Stability Control of monolayer $MoTe_2$ with adsorbed atoms and molecules. *J. Phys. Chem. C* **2015**, *119*, 21674−21680.

(10) Duerloo, K.-A. N.; Li, Y.; Reed, E. J. Structural phase transitions in two-dimensional Mo- and W-dichalcogenide monolayers. *Nat. Commun.* **2014**, *5*, 4214.

(11) Huang, J.-H.; Deng, K.-Y.; Liu, P.-S.; Wu, C.-T.; Chou, C.-T.; Chang, W.-H.; Lee, Y.-J.; Hou, T.-H. Large-area 2D layered $MoTe_2$ by physical vapor deposition and solid-phase crystallization in a tellurium-free atmosphere. *Adv. Mater. Interfaces* **2017**, *4* (17), 1700157.

(12) Zhou, L.; Xu, K.; Zubair, A.; Zhang, X.; Ouyang, F.; Palacios, T.; Dresselhaus, M. S.; Li, Y.; Kong, J. Role of molecular sieves in the CVD synthesis of large-area 2D $MoTe_2$. *Adv. Funct. Mater.* **2017**, *27*, 1603491.

(13) Yoo, Y.; DeGregorio, Z. P.; Su, Y.; Koester, S. J.; Johns, J. E. In-plane 2H-1T′ $MoTe_2$ homojunctions synthesized by flux-controlled phase engineering. *Adv. Mater.* **2017**, *29*, 1605461.

(14) Zhou, L.; Xu, K.; Zubair, A.; Liao, A. D.; Fang, W.; Ouyang, F.; Lee, Y.-H.; Ueno, K.; Saito, R.; Palacios, T.; Kong, J.; Dresselhaus, M. S. Large-area synthesis of high-quality uniform few-layer $MoTe_2$. *J. Am. Chem. Soc.* **2015**, *137*, 11892−11895.

(15) Empante, T. A.; Zhou, Y.; Klee, V.; Nguyen, A. E.; Lu, I. H.; Valentin, M. D.; Naghibi Alvillar, S. A.; Preciado, E.; Berges, A. J.; Merida, C. S.; Gomez, M.; Bobek, S.; Isarraraz, M.; Reed, E. J.; Bartels, L. Chemical vapor deposition growth of few-layer $MoTe_2$ in the 2H, 1T′, and 1T phases: tunable properties of $MoTe_2$ films. *ACS Nano* **2017**, *11*, 900−905.

(16) Park, J. C.; Yun, S. J.; Kim, H.; Park, J.-H.; Chae, S. H.; An, S.-J.; Kim, J.-G.; Kim, S. M.; Kim, K. K.; Lee, Y. H. Phase-engineered synthesis of centimeter-Scale 1T′- and 2H-molybdenum ditelluride thin films. *ACS Nano* **2015**, *9*, 6548−6554.

(17) Yang, L.; Zhang, W.; Li, J.; Cheng, S.; Xie, Z.; Chang, H. Tellurization velocity-dependent metallic-semiconducting-metallic phase evolution in chemical vapor deposition growth of large-area, few-layer $MoTe_2$. *ACS Nano* **2017**, *11*, 1964−1972.

(18) Beams, R.; Cancado, L. G.; Krylyuk, S.; Kalish, I.; Kalanyan, B.; Singh, A. K.; Choudhary, K.; Bruma, A.; Vora, P. M.; Tavazza, F.; Davydov, A. V.; Stranick, S. J. Characterization of few-layer 1T′ $MoTe_2$ by polarization-resolved second harmonic generation and Raman scattering. *ACS Nano* **2016**, *10*, 9626.

(19) Song, Q.; Wang, H.; Pan, X.; Xu, X.; Wang, Y.; Li, Y.; Song, F.; Wan, X.; Ye, Y.; Dai, L. Anomalous in-plane anisotropic Raman response of monoclinic semimetal 1 T′-$MoTe_2$. *Sci. Rep.* **2017**, *7*, 1758.

(20) Ma, X.; Guo, P.; Yi, C.; Yu, Q.; Zhang, A.; Ji, J.; Tian, Y.; Jin, F.; Wang, Y.; Liu, K.; Xia, T.; Shi, Y.; Zhang, Q. Raman scattering in the transition-metal dichalcogenides of 1T′-$MoTe_2$,Td-$MoTe_2$, and Td-WTe_2. *Phys. Rev. B* **2016**, *94*.

(21) Lin, Y. F.; Xu, Y.; Wang, S. T.; Li, S. L.; Yamamoto, M.; Aparecido-Ferreira, A.; Li, W.; Sun, H.; Nakaharai, S.; Jian, W. B.; Ueno, K.; Tsukagoshi, K. Ambipolar $MoTe_2$ transistors and their applications in logic circuits. *Adv. Mater.* **2014**, *26*, 3263−9.

(22) Wang, Y.; Xiao, J.; Zhu, H.; Li, Y.; Alsaid, Y.; Fong, K. Y.; Zhou, Y.; Wang, S.; Shi, W.; Wang, Y.; Zettl, A.; Reed, E. J.; Zhang, X. Structural phase transition in monolayer $MoTe_2$ driven by electrostatic doping. *Nature* **2017**, *550*, 487−491.

(23) Keum, D. H.; Cho, S.; Kim, J. H.; Choe, D.-H.; Sung, H.-J.; Kan, M.; Kang, H.; Hwang, J.-Y.; Kim, S. W.; Yang, H.; Chang, K. J.; Lee, Y. H. Bandgap opening in few-layered monoclinic $MoTe_2$. *Nat. Phys.* **2015**, *11*, 482.

(24) Yamamoto, M.; Wang, S. T.; Ni, M.; Lin, Y.-F.; Li, S.-L.; Aikawa, S.; Jian, W.-B.; Ueno, K.; Wakabayashi, K.; Tsukagoshi, K. Strong enhancement of Raman scattering from a bulk-inactive vibrational mode in few-layer $MoTe_2$. *ACS Nano* **2014**, *8*, 3895−3903.

(25) Guo, H.; Yang, T.; Yamamoto, M.; Zhou, L.; Ishikawa, R.; Ueno, K.; Tsukagoshi, K.; Zhang, Z.; Dresselhaus, M. S.; Saito, R. Double resonance Raman modes in monolayer and few-layer $MoTe_2$. *Phys. Rev. B: Condens. Matter Mater. Phys.* **2015**, *91*, 205415.

(26) Naylor, C. H.; Parkin, W. M.; Ping, J.; Gao, Z.; Zhou, Y. R.; Kim, Y.; Streller, F.; Carpick, R. W.; Rappe, A. M.; Drndić, M.; Kikkawa, J. M.; Johnson, A. T. C. Monolayer single-crystal 1T′-$MoTe_2$ grown by chemical vapor deposition exhibits weak antilocalization effect. *Nano Lett.* **2016**, *16*, 4297−4304.

(27) Bernède, J. C.; Amory, C.; Assmann, L.; Spiesser, M. X-ray photoelectron spectroscopy study of $MoTe_2$ single crystals and thin films. *Appl. Surf. Sci.* **2003**, *219*, 238−248.

(28) Yin, X.; Ye, Z.; Chenet, D. A.; Ye, Y.; O'Brien, K.; Hone, J. C.; Zhang, X. Edge Nonlinear optics on a MoS_2 atomic monolayer. *Science* **2014**, *344*, 488−490.

(29) Zhang, Y. D.; Esling, C.; Lecomte, J. S.; He, C. S.; Zhao, X.; Zuo, L. Grain boundary characteristics and texture formation in a medium carbon steel during its austenitic decomposition in a high magnetic field. *Acta Mater.* **2005**, *53*, 5213−5221.

(30) Carpenter, M. A. Time-temperature-transformation (TTT) analysis of cation disordering in omphacite. *Contrib. Mineral. Petrol.* **1982**, *78*, 433−440.

(31) Porter, D. A.; Easterling, K. E.; Sherif, M. *Phase Transformations in Metals and Alloys, (Revised Reprint)*; CRC Press, 2009.

(32) Li, Y.; Duerloo, K. A.; Wauson, K.; Reed, E. J. Structural semiconductor-to-semimetal phase transition in two-dimensional materials induced by electrostatic gating. *Nat. Commun.* **2016**, *7*, 10671.

(33) Song, S.; Keum, D. H.; Cho, S.; Perello, D.; Kim, Y.; Lee, Y. H. Room temperature semiconductor−metal transition of $MoTe_2$ thin films engineered by strain. *Nano Lett.* **2016**, *16*, 188−193.

DOI: 10.1021/jacs.8b12230
J. Am. Chem. Soc. 2019, 141, 2128−2134